energies

MDPI

Article

A New Active Power Decoupling Cascaded H-Bridge Static Synchronous Compensator and Its Control Method

Qihui Feng [1], Feng Zhu [2], Chenghui Lin [1], Xue Han [1], Dingguo Li [3] and Weilong Xiao [1,*]

[1] Electric Power Research Institute of Guizhou Power Grid Co., Ltd., Guiyang 550002, China; fonqeeh@163.com (Q.F.); lch134@163.com (C.L.); hanxue_gzu@hotmail.com (X.H.)
[2] XJ Electric Co., Ltd., Xuchang 461000, China; zhuizhuosuiyue@163.com
[3] Guiyang Power Supply Bureau of Guizhou Power Grid Co., Ltd., Guiyang 550002, China; 18286004643@163.com
* Correspondence: 19313004590@163.com

Abstract

The cascaded H-bridge static synchronous compensator (STATCOM) has been widely employed in medium- and high-voltage reactive power compensation applications due to its high modularity, fast response speed, and direct grid connection capability. However, the DC-link voltage exhibits an inherent double-frequency ripple, which poses a serious challenge to power quality. Therefore, numerous Active Power Decoupling (APD) techniques have been proposed. However, existing schemes still exhibit certain limitations: independent APD topologies are associated with higher costs, whereas single bridge-arm multiplexed APD topologies are confronted with issues such as elevated DC-side voltage and increased current stress on the multiplexed arm. Consequently, comprehensive optimization is difficult to achieve in terms of the number of power devices, decoupling accuracy, level of capacitor multiplexing, and device stress. To address the above issues, this paper proposes a DC split capacitor (DC-SC)-based dual bridge-arm multiplexed cascaded H-bridge STATCOM with active power decoupling capability, along with its corresponding control method. By constructing a fundamental-frequency common-mode voltage on the decoupling capacitor, this method effectively suppresses the double-frequency ripple in the DC-side voltage and reduces the current stress on the switching devices. The simulation and experimental results have verified the correctness and effectiveness of the proposed topological structure and control method.

Keywords: cascaded H-bridge static synchronous compensator; double-frequency ripple; DC split capacitor; dual bridge-arm multiplexed; active power decoupling; fundamental-frequency common-mode voltage

Check for updates

Academic Editor: Federico Barrero

Received: 4 March 2026
Revised: 2 April 2026
Accepted: 6 April 2026
Published: 8 April 2026

Copyright: © 2026 by the authors. Licensee MDPI, Basel, Switzerland. This article is an open access article distributed under the terms and conditions of the Creative Commons Attribution (CC BY) license.

1. Introduction

In the context of the carbon peaking and carbon neutrality goals, the stability issue of grid voltage is increasingly exacerbated by the large-scale integration of distributed energy resources, such as photovoltaic and wind power [1–3]. The voltage level of the system is directly determined by reactive power balance. Insufficient compensation results in a decrease in grid voltage and an increase in losses [4,5]. The cascaded H-bridge Static Synchronous Compensator (STATCOM) has been widely adopted in medium- and high-voltage reactive power compensation applications, owing to its advantages such as high modularity, rapid response speed, and the capability for direct grid connection [6,7].

However, there is an inherent problem of double-frequency ripple on the DC side [8], which seriously affects the safe operation of the system [9,10].

To suppress the DC-side voltage fluctuation, the most conventional approach involves the adoption of a passive power decoupling scheme with large electrolytic capacitors connected in parallel on the DC side [11]. However, large electrolytic capacitors are prone to defects such as electrolyte evaporation, large size, and short service life, which significantly compromise the reliability of the device [12]. Therefore, various active power decoupling (APD) techniques have been proposed to replace electrolytic capacitors with compact and long-life film capacitors [13,14]. Based on structural forms, APD topologies are classified into isolated and non-isolated types. Isolated APD topologies often utilize forward-flyback and their derived DC/DC structures. Although they exhibit good immunity, they are limited by size and power rating, making them difficult to apply in medium- and high-voltage scenarios [15,16]. Therefore, non-isolated APD topologies have become the research focus.

Existing non-isolated APD topologies can be primarily categorized into two types: the independent type and the switch-multiplexing type. The independent decoupling circuit is integrated into the system as an additional module, with both its topology and control being independent of the main converter [17–24]. In contrast, the switch-multiplexing decoupling circuit shares switching devices with the main circuit, leading to coupling in both structure and control, which necessitates coordinated operation [18]. For independent decoupling topologies, a full-bridge unit is adopted as the APD topology in reference [19], leading to a doubling of the converter volume and a reduction in energy density. In reference [20], a Buck circuit is connected in parallel on the DC side to serve as the decoupling unit. However, its control operates in a semi-open-loop mode, and the calculation of the duty cycle relies on the inductance value, resulting in poor stability and low decoupling accuracy. In references [21,22], Boost and Buck–Boost circuits are employed as decoupling units, respectively. The former exhibits an auxiliary capacitor voltage higher than the DC-side voltage, while the latter is characterized by the highest voltage stress on the switching devices. As a result, both are unsuitable for high-voltage applications [23]. In reference [24], a split-capacitor topology is proposed, which utilizes an independent bridge arm to control the split capacitors. However, since the original converter's switching arms are not involved in the decoupling process, this results in low switch utilization and increased cost.

For the switch-multiplexing decoupling circuit, a Buck circuit-based switch-multiplexing decoupling topology is proposed in reference [25]. However, its control is complex, the response is slow, and the voltage stress on the multiplexed arm is high. In reference [26], a differential Buck decoupling circuit without additional switches is proposed. Although it reduces the voltage stress on the decoupling capacitor, the utilization of the decoupling capacitor is not high, and low-frequency ripple still exists on the DC side. In reference [27], a single-bridge-arm multiplexed APD topology based on the DC-SC circuit is proposed. However, the calculation of the decoupling current reference value depends on the inductance and capacitance parameters, and the voltage stress on the multiplexed arm is high. It is noteworthy that the difference in decoupling accuracy stems from the distinct methods of constructing the common-mode voltage across the decoupling capacitor. In references [20,25,26], a double-frequency common-mode voltage is constructed on the decoupling capacitor. Although this method can provide the required double-frequency ripple power for the system, it inevitably introduces quadruple-frequency ripple, resulting in incomplete decoupling. In contrast, references [24,27] construct a fundamental-frequency common-mode voltage, enabling complete decoupling without generating additional ripple.

In summary, existing active power decoupling methods fail to achieve multi-objective coordinated optimization in terms of the number of power devices, decoupling accuracy, capacitor reuse level, and device current stress, thereby posing challenges in meeting the application requirements of cascaded H-bridge STATCOMs under complex operational conditions. Addressing this research gap will facilitate the reduction in hardware costs and operational stress while maintaining system performance, which is of great significance for advancing the development of high-performance power quality improvement equipment.

Therefore, a topology and its control method for an active power decoupling cascaded H-bridge STATCOM, based on dual bridge-arm multiplexed in the DC-SC circuit, are proposed in this paper. This method effectively suppresses the double-frequency ripple in the DC-side voltage by constructing a fundamental-frequency common-mode voltage on the decoupling capacitor, thereby ensuring decoupling accuracy while reducing device stress and improving the capacitor reuse level. The main contributions of this paper are as follows:

(1) An active decoupling topology based on a dual bridge arm multiplexed in the DC-SC circuit is proposed: without adding extra switching devices, the reuse of the decoupling capacitor and the DC-side support function is achieved, effectively improving the capacitor reuse level and reducing system cost. Meanwhile, the high current stress inherent in single bridge-arm multiplexed configurations is mitigated through the coordinated operation of dual bridge arms.

(2) A decoupling control method based on the fundamental-frequency common-mode voltage is constructed: by generating a fundamental-frequency common-mode decoupling signal combined with a dual-loop control of the decoupling circuit, the double-frequency ripple power is effectively suppressed, thereby avoiding the introduction of additional low-frequency ripples by the double-frequency common-mode decoupling method and consequently enhancing both decoupling accuracy and system stability.

Simulation and experimental results have verified the correctness and effectiveness of the proposed topology and its control method, providing an effective solution for the application of medium- and high-voltage cascaded H-bridge STATCOMs under high-reliability and high-power-quality requirements.

2. Proposed Decoupling Topology and Its Operating Principle

2.1. Topology Structure

Figure 1 shows the main circuit topology of the proposed active power decoupling cascaded H-bridge static synchronous compensator based on dual bridge-arm multiplexed in DC-SC circuits. In Figure 1, the main circuit topology is star-connected and composed of N cascaded cell modules. In the diagram, u_s represents the grid voltage, i_s is the grid current, i_o denotes the STATCOM output current, and i_L signifies the load current. L is the filter inductance. C_{r1} and C_{r3} are the two DC split-capacitors on the left bridge arm, while C_{r2} and C_{r4} are the two DC split-capacitors on the right bridge arm. The currents flowing through C_{r1}, C_{r2}, C_{r3}, and C_{r4} are denoted as i_{cr1}, i_{cr2}, i_{cr3}, and i_{cr4}, respectively. The terminal voltages across C_{r1}, C_{r2}, C_{r3}, and C_{r4} are labeled as u_{c1}, u_{c2}, u_{c3}, and u_{c4}, respectively. L_{r1} and L_{r2} represent the decoupling inductors, with i_{Lr1} and i_{Lr2} indicating their respective currents. The positive directions of all voltages and currents are clearly marked in the figure.

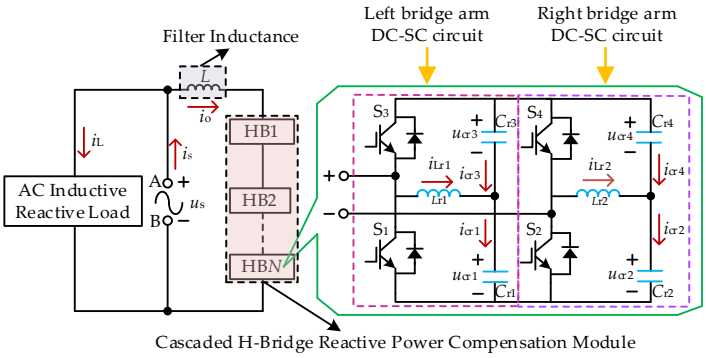


Figure 1. Proposed decoupling main circuit topology.

2.2. Generation Mechanism of Double-Frequency Ripple in DC-Link Voltage

In Figure 1, the expressions for the point of common coupling (PCC) voltage u_s and the STATCOM output current i_o are given by:

$$\begin{cases} u_s = U_s \sin(\omega t + \theta) \\ i_o = I_o \sin(\omega t + \theta + \varphi) \end{cases} \tag{1}$$

In Equation (1), U_s and I_o represent the amplitudes of u_s and i_o, respectively, ω is the fundamental angular frequency of the grid, θ is the initial phase angle of u_s and φ denotes the phase angle of the STATCOM output current i_o relative to the PCC voltage u_s. When compensating for AC inductive reactive loads, $\varphi = \pi/2$.

Thus, the instantaneous power on the AC side can be expressed as

$$p_{ac} = u_s i_o - L\frac{di_o}{dt} i_o = \frac{U_s I_o}{2}\cos\varphi - \frac{U_s I_o}{2}\cos(2\omega t + 2\theta + \varphi) - \frac{\omega L I_o^2}{2}\sin(2\omega t + 2\theta + 2\varphi) \tag{2}$$

The DC voltages of the H-bridge modules are all equal to u_{dc}. When the APD circuit is not activated, the sum of the instantaneous powers on the DC side of each H-bridge module can be expressed as

$$p_{dc} = \frac{NC_d}{2}\frac{du_{dc}^2}{dt} \tag{3}$$

In Equation (3), C_d is the DC-side capacitor of the traditional cascaded H-bridge STATCOM.

Without considering factors such as switching losses, according to the law of conservation of power, by equating Equations (2) and (3), and since the study is conducted in the context of reactive power compensation where $\cos\varphi = 0$, the DC voltage of the H-bridge can be derived as

$$u_{dc} = \sqrt{U_{dc}^2 - \frac{U_s I_o + \omega L I_o^2 \sin\varphi}{2\omega N C_d}\sin(2\omega t + 2\theta + \varphi)} \tag{4}$$

In Equation (4), U_{dc} represents the constant component in the DC voltage of the cascaded H-bridge STATCOM.

The DC voltage of the H-bridge module consists of a constant component and a double-frequency ripple component. This is attributed to the presence of double-frequency ripple power in the instantaneous power on the AC side of the cascaded H-bridge STATCOM, which induces a corresponding ripple in the DC voltage of the H-bridge modules. The ripple magnitude is directly proportional to U_s, I_o, and L. For a given grid voltage level, U_s remains essentially constant, whereas I_o is determined by the compensation capacity. Therefore, with other parameters unchanged, the DC voltage ripple increases with the compensation capacity and becomes more pronounced as the filter inductance increases.

Conversely, the ripple amplitude can be effectively suppressed by appropriately increasing the number of cascaded modules N and the capacitance C_d.

2.3. Working Principle

In Figure 1, the switching devices of the DC-SC circuit are shared with the left and right switching devices of the conventional H-bridge. In addition to realizing the decoupling function, both the left and right bridge arms are required to assist in the power exchange between the AC and DC sides. Based on Figure 1, the equivalent circuit is depicted in Figure 2.

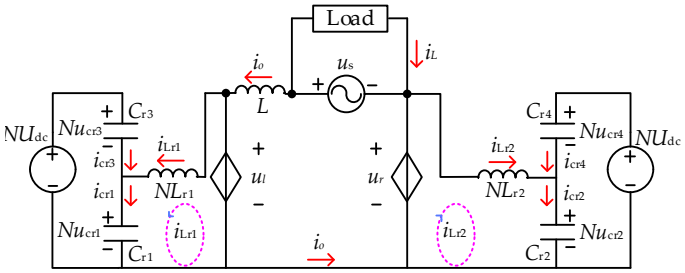


Figure 2. Equivalent circuit of the proposed decoupling main circuit topology.

In Figure 2, N represents the number of cascaded modules, u_l denotes the sum of the output voltages of the left bridge arms, and u_r denotes the sum of the output voltages of the right bridge arms. As shown in Figure 2, the decoupling current i_{Lr1} and the output current i_o flow through the left bridge arm simultaneously, while the decoupling current i_{Lr2} and the output current i_o flow through the right bridge arm simultaneously. Let the AC-side output voltage be u_o. Based on Figure 2, Kirchhoff's Voltage Law (KVL) yields

$$\begin{cases} u_L = L\frac{di_o}{dt} = u_s - u_o \\ u_o = u_l - u_r \\ NL_{rl}\frac{di_{Lr1}}{dt} = u_l - Nu_{cr1} \\ NL_{r2}\frac{di_{Lr2}}{dt} = u_r - Nu_{cr2} \end{cases} \quad (5)$$

As indicated by Equation (5), the decoupling currents i_{Lr1} and i_{Lr2} are regulated by controlling u_l and u_r (i.e., the left and right bridge arms) to suppress ripple. Meanwhile, the output current i_o is jointly determined by u_l and u_r, and its regulation requires coordinated control of the two bridge arms.

2.3.1. Analysis of Decoupling Principle with Equal Capacitances

According to the operating principle of the conventional cascaded H-bridge STATCOM, the output voltages of both the left and right bridge arms should contain a fundamental-frequency voltage component. These two fundamental components have equal amplitudes and are 180 degrees out of phase (differential-mode voltage). Furthermore, to suppress the double-frequency ripple in the DC-side voltage, this can be achieved by adjusting the voltages of the decoupling capacitors. Specifically, identical common-mode voltages are applied to the decoupling capacitor pairs C_{r1} and C_{r2} and C_{r3} and C_{r4}, respectively. Due to the clamping effect of the DC-side voltage, the common-mode voltages across

the upper and lower capacitors within the same bridge arm exhibit opposite polarities. The resulting decoupling capacitor voltages are expressed as follows:

$$\begin{cases} u_{cr1} = \frac{U_{dc}}{2} + U_g \sin(\omega t + \chi) + U_r \sin(\omega t + \delta) \\ u_{cr2} = \frac{U_{dc}}{2} - U_g \sin(\omega t + \chi) + U_r \sin(\omega t + \delta) \\ u_{cr3} = \frac{U_{dc}}{2} - U_g \sin(\omega t + \chi) - U_r \sin(\omega t + \delta) \\ u_{cr4} = \frac{U_{dc}}{2} + U_g \sin(\omega t + \chi) - U_r \sin(\omega t + \delta) \end{cases} \tag{6}$$

In Equation (6), U_{dc} represents the constant value of the DC voltage; U_g and χ are the amplitude and initial phase angle of the differential-mode voltage, respectively; and U_r and δ denote the amplitude and initial phase angle of the common-mode voltage, respectively.

By differentiating Equation (6), the expression for the current flowing through the decoupling capacitor can be directly obtained as follows:

$$\begin{cases} i_{cr1} = C_{r1}\frac{du_{cr1}}{dt} = \omega C_{r1} U_g \cos(\omega t + \chi) + \omega C_{r1} U_r \cos(\omega t + \delta) \\ i_{cr2} = C_{r2}\frac{du_{cr2}}{dt} = -\omega C_{r2} U_g \cos(\omega t + \chi) + \omega C_{r2} U_r \cos(\omega t + \delta) \\ i_{cr3} = C_{r3}\frac{du_{cr3}}{dt} = -\omega C_{r3} U_g \cos(\omega t + \chi) - \omega C_{r3} U_r \cos(\omega t + \delta) \\ i_{cr4} = C_{r4}\frac{du_{cr4}}{dt} = \omega C_{r4} U_g \cos(\omega t + \chi) - \omega C_{r4} U_r \cos(\omega t + \delta) \end{cases} \tag{7}$$

Based on this, the expressions for the currents through the two decoupling inductors can be derived from Kirchhoff's Current Law (KCL) in Figure 2 as follows:

$$\begin{cases} i_{Lr1} = i_{cr1} - i_{cr3} = \omega(C_{r1} + C_{r3}) U_g \cos(\omega t + \chi) + \omega(C_{r1} + C_{r3}) U_r \cos(\omega t + \delta) \\ i_{Lr2} = i_{cr2} - i_{cr4} = -\omega(C_{r2} + C_{r4}) U_g \cos(\omega t + \chi) + \omega(C_{r2} + C_{r4}) U_r \cos(\omega t + \delta) \end{cases} \tag{8}$$

To simplify the analysis, parameter deviations caused by factors such as production variations and capacitor aging are temporarily neglected. It is assumed that the parameters of the decoupling inductors and capacitors remain consistent, specifically, $L_{r1} = L_{r2} = L_r$ and $C_{r1} = C_{r2} = C_{r3} = C_{r4} = C_r$. Under these conditions, the output voltage u_o can be derived by combining Equations (5), (6) and (8) as follows:

$$u_o = 2NU_g(1 - 2\omega^2 L_r C_r)\sin(\omega t + \chi) \tag{9}$$

To minimize the capacitance and inductance values as much as possible, thereby reducing system cost, and under the constraint $L_r C_r < 1/2\omega^2$, the amplitude and initial phase angle of the differential-mode voltage on the decoupling capacitors can be derived by combining Equations (5) and (9) as follows:

$$\begin{cases} \chi = \theta \\ U_g = \frac{U_s + \omega L I_o}{2N(1 - 2\omega^2 L_r C_r)} \end{cases} \tag{10}$$

Let the instantaneous power consumed by the decoupling capacitors be denoted as p_{cr1}, p_{cr2}, p_{cr3}, p_{cr4} and the instantaneous power consumed by the decoupling inductors as p_{Lr1} and p_{Lr2}. The total instantaneous power of the decoupling circuit can then be derived by combining Equations (6) and (8) as follows:

$$\begin{aligned} p_{dc} &= N(p_{crl} + p_{cr2} + p_{cr3} + p_{cr4} + p_{Lrl} + p_{Lr2}) = N(i_{crl}u_{crl} + i_{cr2}u_{cr2} + i_{cr3}u_{cr3} + i_{cr4}u_{cr4} + L_r\frac{di_{Lrl}}{dt}i_{Lrl} + L_r\frac{di_{Lr2}}{dt}i_{Lr2}) \\ &= N(2\omega C_r U_g^2 - 4\omega^3 L_r C_r^2 U_g^2)\sin(2\omega t + 2\chi) + N(2\omega C_r U_r^2 - 4\omega^3 L_r C_r^2 U_r^2)\sin(2\omega t + 2\delta) \end{aligned} \tag{11}$$

Under reactive power compensation operating conditions, the instantaneous power expression (2) on the AC side can be further simplified as

$$p_{ac} = \frac{1}{2}(U_s I_o + \omega L I_o^2)\sin(2\omega t + 2\theta) \tag{12}$$

To suppress the double-frequency voltage fluctuation on the DC side of the proposed novel cascaded H-bridge STATCOM and transfer the oscillating power, the double-frequency ripple power terms in Equations (11) and (12) are set to be equal. Then, by incorporating Equation (10), the amplitude and initial phase angle of the fundamental-frequency common-mode voltage to be constructed across the decoupling capacitors can be determined as follows:

$$\begin{cases} \delta = \theta - \frac{\pi}{2} \\ U_{\mathrm{r}} = \frac{1}{2}\sqrt{\frac{(U_{\mathrm{s}}+\omega L I_{\mathrm{o}})^2}{N^2(1-2\omega^2 L_{\mathrm{r}} C_{\mathrm{r}})^2} - \frac{U_{\mathrm{s}} I_{\mathrm{o}}+\omega L I_{\mathrm{o}}^2}{N\omega C_{\mathrm{r}}(1-2\omega^2 L_{\mathrm{r}} C_{\mathrm{r}})}} \end{cases} \tag{13}$$

In summary, by implementing specific control strategies to ensure the decoupling capacitor voltages satisfy Equations (6), (10) and (13), the double-frequency power in the system can be compensated, thereby effectively suppressing the DC-side voltage ripple in the proposed novel cascaded H-bridge STATCOM.

2.3.2. Differential Analysis with Unequal Capacitances

It is assumed that the decoupling capacitance values are all unequal, i.e., $C_{\mathrm{r1}} \neq C_{\mathrm{r2}} \neq C_{\mathrm{r3}} \neq C_{\mathrm{r4}}$. Under this condition, the form of the capacitor voltage prior to decoupling remains consistent with Equation (6), while the capacitor currents differ due to the variations in capacitance values.

Since both the differential-mode voltage and common-mode voltage in Equation (6) are fundamental-frequency voltages, and U_{dc} is a constant DC voltage, it can be inferred from the forms of decoupling capacitor voltages and currents under different capacitance values that the combination of the DC voltage component and the fundamental-frequency current component results in fundamental-frequency reactive power. This fundamental-frequency energy causes fundamental-frequency voltage fluctuations on the DC side of the cascaded H-bridge STATCOM. When the fluctuating power is transmitted to the AC side, it introduces a DC offset and second-order harmonics in the output current, thereby compromising power quality. The decoupling system ensures the conservation of double-frequency power, while the presence of fundamental-frequency power is prohibited after decoupling. By combining Equations (6) and (7), the expression for the fundamental-frequency power under four different capacitance values of the decoupling capacitors is derived as follows:

$$\begin{cases} P_{\mathrm{cr1}(\omega)} = \frac{\omega C_{\mathrm{r1}} U_{\mathrm{g}} U_{\mathrm{dc}}}{2}\cos(\omega t+\chi) + \frac{\omega C_{\mathrm{r1}} U_{\mathrm{r}} U_{\mathrm{dc}}}{2}\cos(\omega t+\delta) \\ P_{\mathrm{cr2}(\omega)} = -\frac{\omega C_{\mathrm{r2}} U_{\mathrm{g}} U_{\mathrm{dc}}}{2}\cos(\omega t+\chi) + \frac{\omega C_{\mathrm{r2}} U_{\mathrm{r}} U_{\mathrm{dc}}}{2}\cos(\omega t+\delta) \\ P_{\mathrm{cr3}(\omega)} = -\frac{\omega C_{\mathrm{r3}} U_{\mathrm{g}} U_{\mathrm{dc}}}{2}\cos(\omega t+\chi) - \frac{\omega C_{\mathrm{r3}} U_{\mathrm{r}} U_{\mathrm{dc}}}{2}\cos(\omega t+\delta) \\ P_{\mathrm{cr4}(\omega)} = \frac{\omega C_{\mathrm{r4}} U_{\mathrm{g}} U_{\mathrm{dc}}}{2}\cos(\omega t+\chi) - \frac{\omega C_{\mathrm{r4}} U_{\mathrm{r}} U_{\mathrm{dc}}}{2}\cos(\omega t+\delta) \end{cases} \tag{14}$$

By summing the fundamental-frequency powers in Equation (14) and setting the sum to zero, the following is obtained:

$$\begin{aligned} P_{\mathrm{c1}(\omega)} + P_{\mathrm{c2}(\omega)} + P_{\mathrm{c3}(\omega)} + P_{\mathrm{c4}(\omega)} = {} & \omega U_{\mathrm{g}} U_{\mathrm{dc}} \cdot \frac{C_{\mathrm{rl}}+C_{\mathrm{r4}}-C_{\mathrm{r2}}-C_{\mathrm{r3}}}{2}\cos(\omega t+\chi) \quad + \\ & \omega U_{\mathrm{r}} U_{\mathrm{dc}} \cdot \frac{C_{\mathrm{rl}}+C_{\mathrm{r2}}-C_{\mathrm{r3}}-C_{\mathrm{r4}}}{2}\cos(\omega t+\delta) = 0 \end{aligned} \tag{15}$$

Consequently, it can be derived that

$$\begin{cases} C_{\mathrm{rl}} + C_{\mathrm{r4}} = C_{\mathrm{r2}} + C_{\mathrm{r3}} \\ C_{\mathrm{rl}} + C_{\mathrm{r2}} = C_{\mathrm{r3}} + C_{\mathrm{r4}} \end{cases} \tag{16}$$

Therefore, to prevent the generation of fundamental-frequency power, the conditions $C_{r1} = C_{r3}$ and $C_{r2} = C_{r4}$ must be satisfied. This implies that only the capacitances on opposite sides are permitted to differ, i.e., $C_{r1} \neq C_{r2}$ and $C_{r3} \neq C_{r4}$, under which the solution of the double-frequency power balance equation for the system becomes relatively complex. This study focuses on the functionality of the decoupling circuit topology, and thus the discussion is confined to scenarios where the decoupling capacitors possess identical capacitance values.

3. Circuit Decoupling Control Strategy

3.1. Analysis of Modulation Requirements for Circuit Decoupling

Modulation serves as the pivotal element that determines whether a multiplexing circuit can achieve decoupling functionality. A thorough analysis of its operational mechanism is crucial for understanding the working principles of this circuit.

Based on Equation (8), the voltage drops across the two decoupling inductors can be derived, respectively, as

$$\begin{cases} u_{Lr1} = L_r \frac{di_{Lr1}}{dt} = -2\omega^2 L_r C_r U_g \sin(\omega t + \chi) - 2\omega^2 L_r C_r U_r \sin(\omega t + \delta) \\ u_{Lr2} = L_r \frac{di_{Lr2}}{dt} = 2\omega^2 L_r C_r U_g \sin(\omega t + \chi) - 2\omega^2 L_r C_r U_r \sin(\omega t + \delta) \end{cases} \tag{17}$$

Given the switching functions S_L and S_R for the left and right bridge arms, respectively, as defined in Figure 2, it follows that:

$$\begin{cases} u_l = \frac{NU_{dc}}{2} S_L + \frac{NU_{dc}}{2} \\ u_r = \frac{NU_{dc}}{2} S_R + \frac{NU_{dc}}{2} \end{cases} \tag{18}$$

From Equations (5) and (18), it can be observed that the decoupling currents i_{Lr1} and i_{Lr2}, as well as the output current i_o, are simultaneously influenced by the switching functions S_L and S_R. Therefore, effective control of the aforementioned currents is achieved through coordinated regulation of the left and right bridge arms. During the analysis, the high-order harmonics in the switching function are neglected and are typically approximated by the corresponding modulation waves. Let m_L and m_R denote the modulation waves of the left and right bridge arms, respectively. By combining Equations (5), (17) and (18), the following can be further derived:

$$\begin{cases} m_L = S_L = \frac{2(U_g - 2\omega^2 L_r C_r U_g)}{U_{dc}} \sin(\omega t + \chi) + \frac{2(U_r - 2\omega^2 L_r C_r U_r)}{U_{dc}} \sin(\omega t + \delta) \\ m_R = S_R = -\frac{2(U_g - 2\omega^2 L_r C_r U_g)}{U_{dc}} \sin(\omega t + \chi) + \frac{2(U_r - 2\omega^2 L_r C_r U_r)}{U_{dc}} \sin(\omega t + \delta) \end{cases} \tag{19}$$

The modulation wave corresponding to the output voltage is defined as m_o. Since both bridge arms are involved in the power exchange between the AC and DC sides, the following is obtained:

$$m_o = \frac{m_L - m_R}{2} = \frac{2U_g(1 - 2\omega^2 L_r C_r)}{U_{dc}} \sin(\omega t + \chi) \tag{20}$$

By combining Equations (10), (13), (19) and (20), the specific expressions for the left and right bridge arm modulation waves and the output voltage modulation wave can be derived as follows:

$$\begin{cases} m_{\mathrm{L}} = \frac{U_{\mathrm{s}}+\omega LI_{\mathrm{o}}}{NU_{\mathrm{dc}}}\sin(\omega t+\theta) - \\ \frac{1}{U_{\mathrm{dc}}}\sqrt{\frac{(U_{\mathrm{s}}+\omega LI_{\mathrm{o}})^2}{N^2} - \frac{(U_{\mathrm{s}}I_{\mathrm{o}}+\omega LI_{\mathrm{o}}^2)(1-2\omega^2L_{\mathrm{r}}C_{\mathrm{r}})}{N\omega C_{\mathrm{r}}}}\cos(\omega t+\theta) \\ m_{\mathrm{R}} = -\frac{U_{\mathrm{s}}+\omega LI_{\mathrm{o}}}{NU_{\mathrm{dc}}}\sin(\omega t+\theta) - \\ \frac{1}{U_{\mathrm{dc}}}\sqrt{\frac{(U_{\mathrm{s}}+\omega LI_{\mathrm{o}})^2}{N^2} - \frac{(U_{\mathrm{s}}I_{\mathrm{o}}+\omega LI_{\mathrm{o}}^2)(1-2\omega^2L_{\mathrm{r}}C_{\mathrm{r}})}{N\omega C_{\mathrm{r}}}}\cos(\omega t+\theta) \\ m_{\mathrm{o}} = \frac{U_{\mathrm{s}}+\omega LI_{\mathrm{o}}}{NU_{\mathrm{dc}}}\sin(\omega t+\theta) \end{cases} \tag{21}$$

3.2. Overall Control Strategy

Based on the preceding analysis, Equations (19) and (20) indicate that in the proposed decoupling main circuit, the left bridge arm modulation wave m_{L} can be expressed as the output voltage modulation wave m_{o} superimposed with a fundamental-frequency modulation wave m_{ω} generated for constructing the common-mode voltage. The right bridge arm modulation wave m_{R} is composed of m_{o} superimposed with m_{ω}. The modulation wave m_{o} is obtained by regulating the output current i_{o} to achieve reactive power compensation, whereas m_{ω} is generated by controlling the sum $i_{\mathrm{Lr1}} + i_{\mathrm{Lr2}}$ to produce the required common-mode voltage for power decoupling. Based on this analysis, independent closed-loop control systems can be designed for the common-mode decoupling circuit and the reactive power compensation output circuit of the proposed topology, thereby achieving coordinated operation of the two functional parts.

Figure 3 shows the schematic diagram of the overall control strategy for the proposed novel cascaded H-bridge STATCOM. It can be observed that the output voltage modulation wave can be obtained through the dual-loop voltage-current control strategy conventionally used in cascaded H-bridge STATCOMs. This control structure consists of an outer voltage loop controller and an inner current loop controller, with the output current reference derived from both the DC-link voltage control and the load reactive current.

The fundamental-frequency common-mode decoupling signal is obtained using a dual-loop control scheme applied to the decoupling circuit. This control method achieves power decoupling by regulating the decoupling inductor current such that the voltage ripple across the decoupling capacitor is maintained at the fundamental frequency. Equation (8) shows that the currents i_{Lr1} and i_{Lr2} contain only fundamental-frequency components; therefore, their reference values must also be fundamental-frequency signals. However, the DC-link voltage ripple of the cascaded H-bridge STATCOM exhibits a double-frequency characteristic and should therefore be converted into a fundamental-frequency component. Based on the frequency-reduction principle of the rotation matrix, the DC-link voltage feedback value u_{dcv} of the cascaded H-bridge STATCOM is first subtracted from its reference value u_{dcv}*. The resulting error is then processed through phase-delayed frequency reduction. The output of the frequency-reduction matrix contains not only the required fundamental-frequency component but also a minor third-harmonic component. Consequently, a resonance controller (RC) is employed to extract the desired fundamental-frequency signal, which serves as the reference for the decoupling inductor current. The expression for the frequency-reduction matrix T is given by:

$$T = \begin{bmatrix} \cos\omega t & \sin\omega t \\ -\sin\omega t & \cos\omega t \end{bmatrix} \tag{22}$$

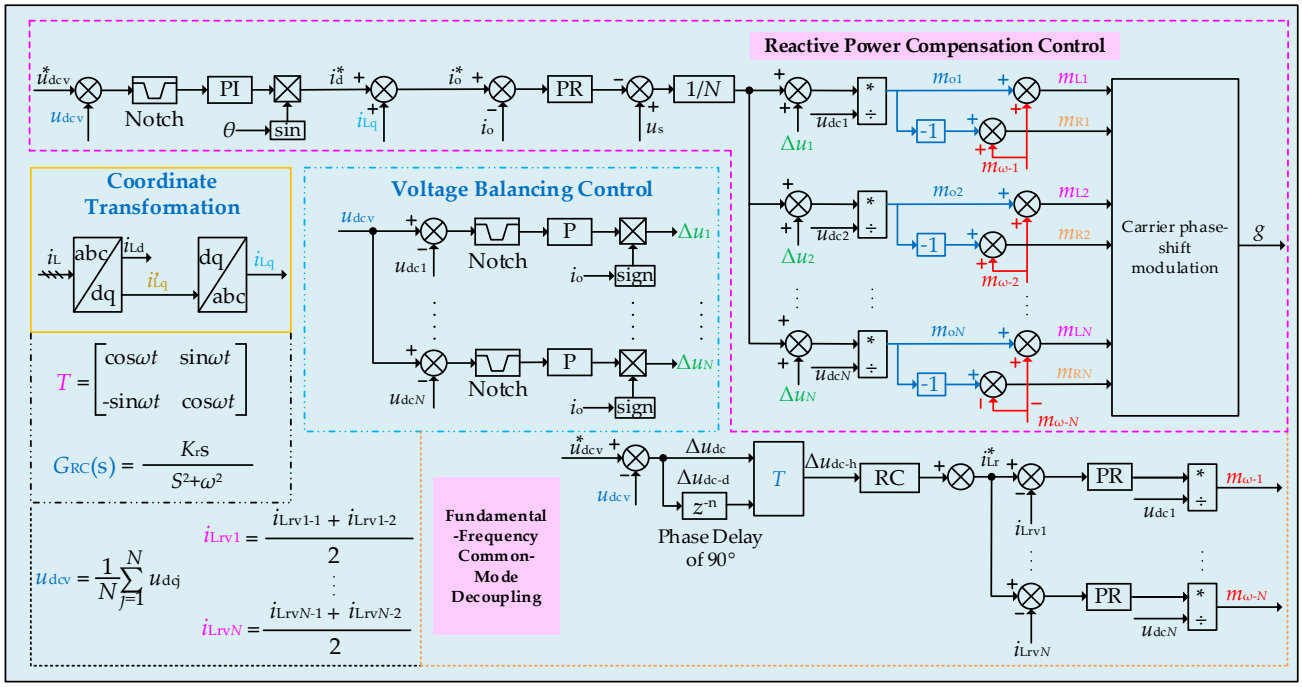


Figure 3. Schematic diagram of the overall control strategy for the proposed novel cascaded H-bridge STATCOM.

Based on the control principle illustrated in Figure 3, integrated with the unipolar double-frequency carrier phase-shift modulation technique, the overall control of the proposed novel cascaded H-bridge STATCOM can be achieved.

The control strategy in this paper features an independent design for reactive power compensation and fundamental-frequency common-mode decoupling. Its control architecture adopts a combined approach integrating the traditional dual-loop voltage-current control of cascaded H-bridge STATCOM with a dual-loop decoupling control circuit. The reactive power control segment adopts a well-established control framework, while the decoupling control part achieves power decoupling by constructing a fundamental-frequency common-mode modulation waveform. Compared to traditional control structures, although this paper introduces an additional decoupling current closed-loop control, this loop exhibits a well-defined linear transfer function with respect to the controlled object (decoupling inductor current). This characteristic facilitates parameter tuning using classical frequency-domain methods, ensuring practical engineering operability.

In terms of sensing requirements, to achieve fast response for fundamental-frequency common-mode decoupling, this work adds an inner current loop to the outer voltage loop, which requires the addition of two additional inductor current sensors. Generally, most cascaded H-bridge STATCOM decoupling schemes require a greater number of sensors than the basic converter when simultaneously addressing both reactive power compensation and decoupling control. However, for the control of different decoupling schemes, employing single-loop control for distinct functional modules remains a viable option. The primary differences lie in dynamic response and the quantity of sensors needed, which conversely provides a relatively high degree of design flexibility.

This work effectively suppresses the double-frequency ripple power in the DC-side voltage by constructing a fundamental-frequency common-mode voltage across the decoupling capacitor. Both theoretical analysis and experimental results demonstrate that the proposed method achieves high decoupling accuracy. Meanwhile, the proposed scheme requires no additional switching devices and effectively reduces both the capacitor capacitance and device stress, achieving a favorable balance between performance and cost.

However, this performance improvement is achieved at the expense of increased control complexity and additional sensors. Nonetheless, in medium- to high-voltage STATCOM applications where high reliability is pursued, this trade-off holds practical engineering significance, particularly aligning with the current demands for high power quality.

4. Design of Decoupling Capacitor Parameters and Analysis of Voltage/Current Stresses

4.1. Design Method for Decoupling Capacitor Parameters

As indicated by Equations (6), (10) and (13), under given conditions of grid voltage level, number of cascaded modules, and reactive power compensation, the voltage ripple across the decoupling capacitor is solely determined by its capacitance value if the influence of the decoupling inductor and filter inductor is neglected. Assuming U_{fluct} as the amplitude of the decoupling capacitor voltage ripple, and based on Equations (10) and (13), the expression for the voltage ripple amplitude in Equation (6) can be simplified to

$$U_{\text{fluct}} = \sqrt{\left(\frac{U_{\text{s}}}{2N}\right)^2 + \frac{U_{\text{s}}^2}{4N^2} - \frac{U_{\text{s}} I_{\text{o}}}{4N\omega C_{\text{r}}}} \tag{23}$$

From the constraints of the modulation conditions, it follows that

$$U_{\text{fluct}} \leq \frac{U_{\text{dc}}}{2} \tag{24}$$

By combining Equations (23) and (24), the ideal decoupling capacitance value is obtained as

$$C_{\text{r}} \leq \frac{N U_{\text{s}} I_{\text{o}}}{2\omega U_{\text{s}}^2 - \omega N^2 U_{\text{dc}}^2} \tag{25}$$

For comparison with the capacitance value of a conventional cascaded H-bridge STATCOM, let the DC-side capacitance of the conventional cascaded H-bridge STATCOM be denoted as C_{d}. The expression for it is derived as

$$C_{\text{d}} = \frac{(1+\varepsilon) U_{\text{s}} I_{\text{o}}}{2N\omega\lambda_{\text{d}} U_{\text{dc}}^2} \tag{26}$$

In Equation (26) λ_{d} represents the allowable ripple range of the DC-side voltage, typically selected as 5% to 10% of U_{dc}, while ε denotes a margin coefficient generally set between 0 and 0.2.

To compare the difference in DC-side capacitance values between the conventional and the proposed novel cascaded H-bridge STATCOM, based on the given system parameters and according to Equations (25) and (26), the capacitance value as a function of the DC voltage is plotted in Figure 4, where λ_{d} is set to 5% and ε to 0.2.

According to the results shown in Figure 4, while preventing over-modulation in the bridge arms and maintaining the DC voltage at a relatively low level, the proposed decoupling circuit for double-frequency ripple suppression can reduce the required capacitance by approximately six-sevenths compared with the conventional cascaded H-bridge STATCOM. Specifically, even if each decoupling capacitor is set to the maximum allowable value in the design, the total capacitance of the four decoupling capacitors is 3.2 mF, which is still only three-fifths of that required by the conventional structure. This demonstrates that the proposed topology can replace large electrolytic capacitors in conventional solutions with small-value film capacitors, thereby achieving the same ripple suppression effect while significantly improving the operational reliability of the system.

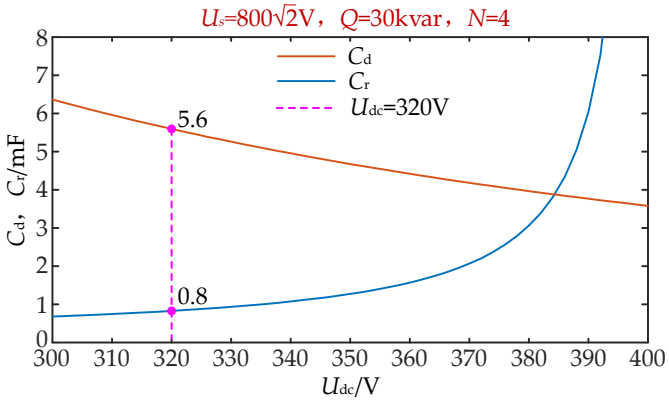


Figure 4. Variation in capacitance value with DC voltage.

4.2. Voltage and Current Stress Analysis

Figure 5 shows the simulated waveforms of the decoupling capacitor voltages u_{cr1}, u_{cr2}, u_{cr3}, and u_{cr4} in the proposed novel cascaded H-bridge STATCOM after the construction of fundamental-frequency common-mode voltage decoupling.

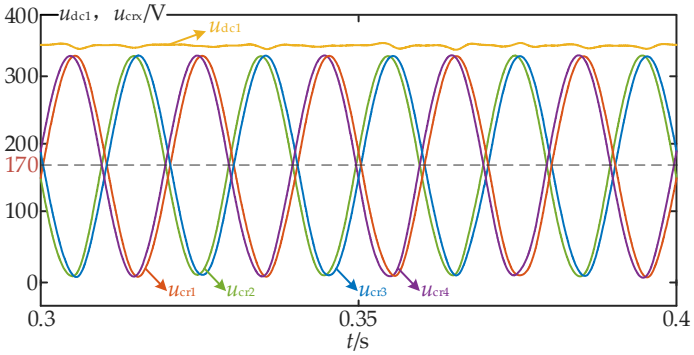


Figure 5. Simulated waveforms of decoupling capacitor voltages.

The waveform agrees with the expression derived by substituting the results from Equations (10) and (13) into Equation (6). The voltage stress on each decoupling capacitor is equal, with a voltage fluctuation range of 8 V to 332 V, meeting the constraints of the modulation conditions. When selecting the voltage rating of the decoupling capacitors, the amplitude of the capacitor voltage after decoupling must be taken into account to determine the appropriate capacitor model, thereby preventing the arm output voltage from exceeding the tolerable range of the capacitors.

As can be seen from Figure 2, the left bridge arm simultaneously carries the decoupling current i_{Lr1} and the output current i_o, while the right bridge arm simultaneously carries the decoupling current i_{Lr2} and the output current i_o. According to Equations (8), (10) and (13), under ideal conditions, the two decoupling currents have equal amplitudes. Therefore, the current stress on the switches in the left and right bridge arms is identical. Consequently, the current stress analysis will be performed using the left bridge arm switch as an example.

By combining Equations (1), (8), (10) and (13), the boundary value of the current i_l flowing through the left bridge arm can be obtained as:

$$i_l = i_o - i_{Lr1} = (I_o - \frac{\omega C_r(U_s + \omega L I_o)}{N(1 - 2\omega^2 L_r C_r)})\cos(\omega t + \theta) - \sqrt{\left[\frac{\omega C_r(U_s + \omega L I_o)}{N(1 - 2\omega^2 L_r C_r)}\right]^2 - \frac{\omega C_r(U_s I_o + \omega L I_o^2)}{N(1 - 2\omega^2 L_r C_r)}}\sin(\omega t + \theta) \quad (27)$$

Figure 6 shows the simulated waveforms of the output current, decoupling inductor current, and left bridge arm current, along with the corresponding theoretical waveforms calculated from Equations (1), (8) and (27).

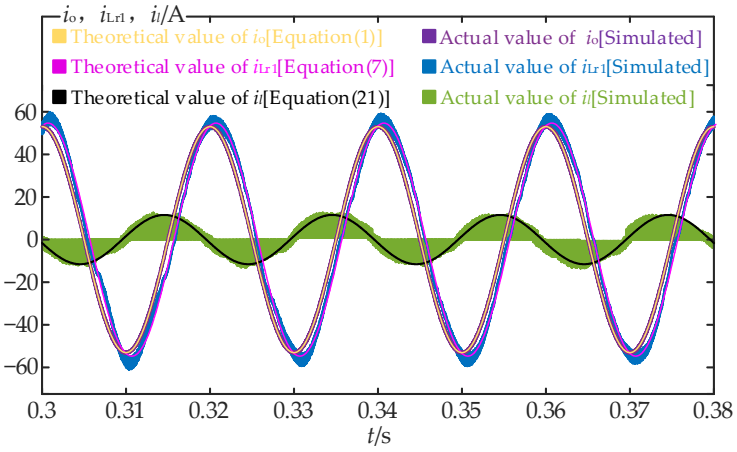


Figure 6. Proposed current simulation waveforms and theoretical waveforms.

In the figure, the "Actual Value" refers to the current waveform obtained through time-domain simulation of the proposed circuit using simulation software (Matlab/Simulink R2024a). It reflects the actual operational behavior of the system under the given parameter conditions. The "Theoretical Value" refers to the current waveform calculated based on the analytical expressions derived in this paper. It represents the mathematical description of the circuit under idealized assumptions (such as neglecting switch voltage drops, parasitic parameters, etc.). The two values originate from different sources: the actual value is derived from the solution of the simulation model, while the theoretical value is obtained from calculations using analytical formulas.

The comparison between the simulated and theoretical waveforms in Figure 6 shows good agreement, verifying the established mathematical model and theoretical analysis. In the figure, the current amplitude of the left bridge arm is lower than that of the output current, indicating reduced current stress on the switching devices in the proposed cascaded H-bridge STATCOM compared with the conventional topology. Consequently, this reduction provides a distinct advantage in device selection. Furthermore, the current rating of the decoupling inductor should be determined based on the amplitude of the decoupled inductor current.

5. Comparative Analysis of Schemes

5.1. Classification and Comparison of APD Topologies in Medium- and High-Voltage Applications

Currently, typical APD topologies suitable for medium- and high-voltage applications mainly fall into two categories: the Buck-type and the DC-SC-type topologies. According to the degree of switch-multiplexing in their circuit structures, they can be classified into three types: the independent topology, the single bridge-arm multiplexed topology, and the dual bridge-arm multiplexed topology. Currently, the widely adopted power decoupling solution for STATCOMs achieves its core function by generating fundamental or double-frequency common-mode voltages across the decoupling capacitor to compensate for the required double-frequency ripple power in the system. The following analysis primarily presents a diversified comparison of topological structures and decoupling accuracy, categorized according to the degree of switching device sharing.

Reference [20] adopts an independent APD topology based on the Buck circuit; Reference [25] employs a multiplexing APD topology derived from the Buck circuit; Reference [26] utilizes an APD topology structured on a differential Buck circuit; Reference [24] implements an independent APD topology grounded in the DC-SC circuit; and reference [27] applies a single bridge-arm multiplexed APD topology based on the DC-SC circuit. Based on these schemes, the detailed analysis and comparison are as follows.

The solutions proposed in references [20,25,26] all achieve power decoupling by generating a double-frequency common-mode voltage across the decoupling capacitor. However, although this method can supply the required double-frequency power to the system, it simultaneously introduces an undesirable quadruple-frequency ripple power component, resulting in incomplete decoupling. Moreover, the aforementioned solutions all require additional support capacitors to be installed on the DC side, increasing both system cost and volume.

In contrast, the solutions proposed in references [24,27] achieve complete power decoupling by generating a fundamental-frequency common-mode voltage across the decoupling capacitor, without requiring additional support capacitors on the DC side. However, the independent APD topology adopted in references [20,24] requires two additional switching devices, increasing system cost and resulting in lower cost-effectiveness. In contrast, the single bridge-arm multiplexed APD topology employed in references [25,27] while eliminating the need for additional switching devices, subjects the shared switches to higher voltage stress, resulting in a lower DC-side voltage utilization ratio.

In comparison, the dual bridge-arm multiplexed APD topology based on the DC-SC circuit proposed in this paper also achieves complete power decoupling by generating a fundamental-frequency common-mode voltage across the decoupling capacitor. Without adding extra switching devices, this topology reuses both bridge arms of the DC-SC circuit. Via the clamping effect of the DC-side voltage, it cancels the fundamental-frequency power component generated by the split capacitors, thereby retaining the required double-frequency power component for the system. Based on Table 1, it can be inferred that the optimal topology must satisfy the following conditions: a minimum number of additional switching devices, low voltage stress on the switching devices, low current stress on the switching devices of the reused bridge arm, and high decoupling accuracy. The novel cascaded H-bridge static synchronous compensator proposed in this paper exhibits significant advantages in the aforementioned indicators. Moreover, the capacitance of the decoupling capacitors is markedly reduced, and their distribution is more centralized, resulting in superior comprehensive performance.

5.2. Comparative Analysis of Decoupling Capacitor Reuse Hierarchy in APD Topologies

When comparing different APD topologies in medium- and high-voltage applications, capacitors act as the primary passive components for decoupling in the system. In this analysis, capacitors serve two main functions: decoupling and DC-side voltage support. Topologies with higher levels of capacitor reuse reduce the volume of passive components and improve cost-effectiveness. This section conducts a hierarchical analysis of the decoupling capacitor reuse among the main topology types introduced Section 4.1, with statistical results summarized in Table 2.

Table 1. Diversified comparison of typical APD topologies for medium- and high-voltage applications.

References	Types of Common-Mode Voltage in Decoupling Circuits	Number of Switching Devices	Number of Additional Switching Devices	Voltage Stress Across the Switching Devices	Current Stress on the Switching Devices in the Reused Bridge Arm	C_r/C_d	Number of PI and PR Controllers	Decoupling Algorithm Accuracy
[20]	double-frequency	6	2	U_{dc}	/	1/10	3	Residual quadruple-frequency ripple
[25]	double-frequency	4	0	$2U_{dc}$	$>I_o$	1/2.5	5	Residual quadruple-frequency ripple
[26]	double-frequency	4	0	U_{dc}	$<I_o$	1/5	4	Residual quadruple-frequency ripple
[24]	Fundamental-frequency	6	2	U_{dc}	/	1/5	2	Complete Decoupling
[27]	Fundamental-frequency	4	0	$2U_{dc}$	$>I_o$	1/2.5	4	Complete Decoupling
Proposed Topology	Fundamental-frequency	4	0	U_{dc}	$<I_o$	1/7	4	Complete Decoupling

Table 2. Decoupling capacitor reuse hierarchy statistics.

References	Decoupling/DC-Side Support	Reuse Hierarchy Level
[20]	1/0	1
[25]	1/0	1
[26]	1/0	1
[24]	1/1	2
[27]	1/1	2
Proposed Topology	1/1	2

As shown in Table 2, the proposed topology achieves the highest level of capacitor reuse, whereas other schemes exhibit lower reuse levels with inherent limitations: some require additional power switches, while others experience increased voltage stress due to switch multiplexing. Furthermore, the topologies in references [20,25,26] require additional capacitive components to compensate for insufficient decoupling, which limits the integrated design of passive system components.

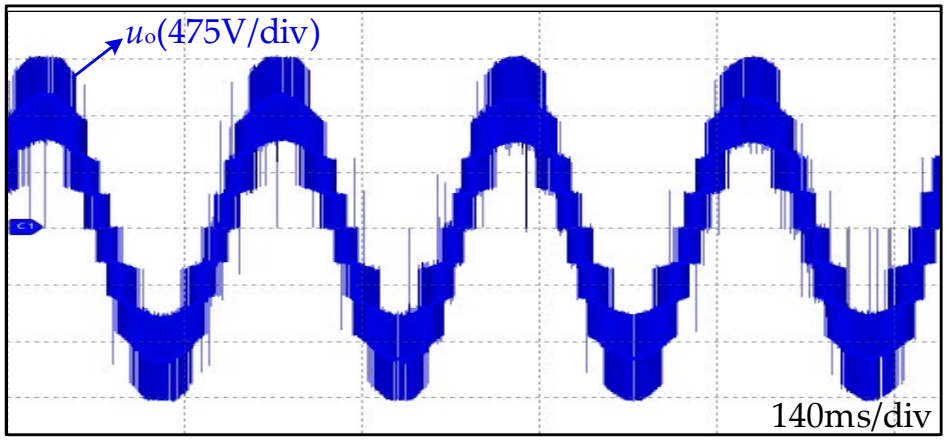
6. Experimental Results and Analysis

Experiments were conducted to verify the decoupling performance of the proposed novel cascaded H-bridge static synchronous compensator and the effectiveness of its control method. Specific experimental parameters are listed in Table 3.

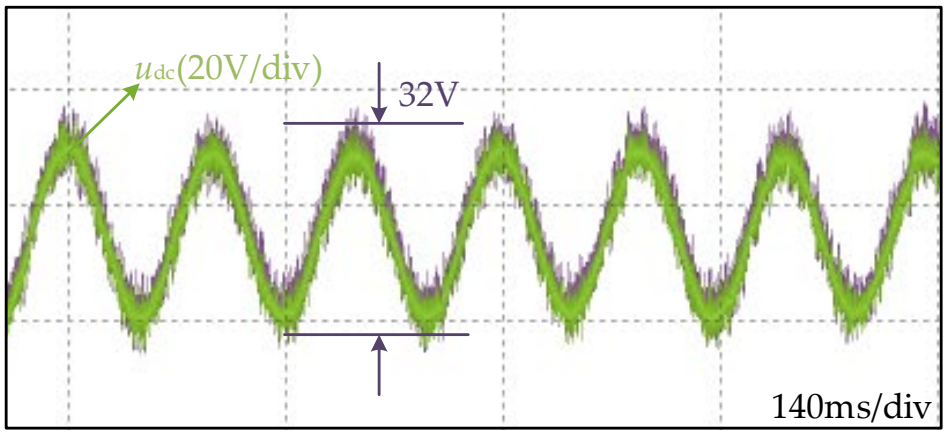
Figure 7 shows the experimental output waveforms of the conventional cascaded H-bridge static synchronous compensator under the same conditions as the proposed novel compensator (with a DC-side capacitance of Cd = 2.16 mF). As can be seen, the DC-side voltage u_{dc} exhibits a significant double-frequency ripple with a range of 32 V, which is close to 10% of the DC voltage. Consequently, affected by the double-frequency ripple in the DC-side voltage, the quality of the nine-level output voltage u_o on the AC side is noticeably degraded.

Table 3. Experimental parameters of the proposed novel cascaded H-Bridge static synchronous compensator.

Parameters	Symbol	Value
AC Grid phase-voltage	U_s	$800\sqrt{2}$ V
Grid frequency	f_0	50 Hz
Compensation capacity	Q	30 kvar
Filter inductor	L	3 mH
Switching frequency	f_{hb}	3 kHz
DC input voltage	U_{dc}	340 V
Decoupling capacitor	C_r	0.54 mF
Decoupling inductor	L_r	0.7 mH
Number of cascaded modules	N	4
Grid initial phase angle	θ	0



（a）



（b）

Figure 7. Experimental output waveforms of conventional cascaded H-Bridge STATCOM. (**a**) DC-side voltage experimental waveform. (**b**) Experimental waveform of AC-side output voltage.

Based on the experimental parameters in Table 3, the results are shown in Figure 8. In the experimental waveforms, u_{dcx} (x = 1, 2, 3, 4) represents the DC-side voltage of each module in the cascaded H-bridge STATCOM, i_o is the output current, u_s is the grid voltage, i_s is the grid current, and u_o is the AC-side output voltage of the cascaded H-bridge STATCOM.

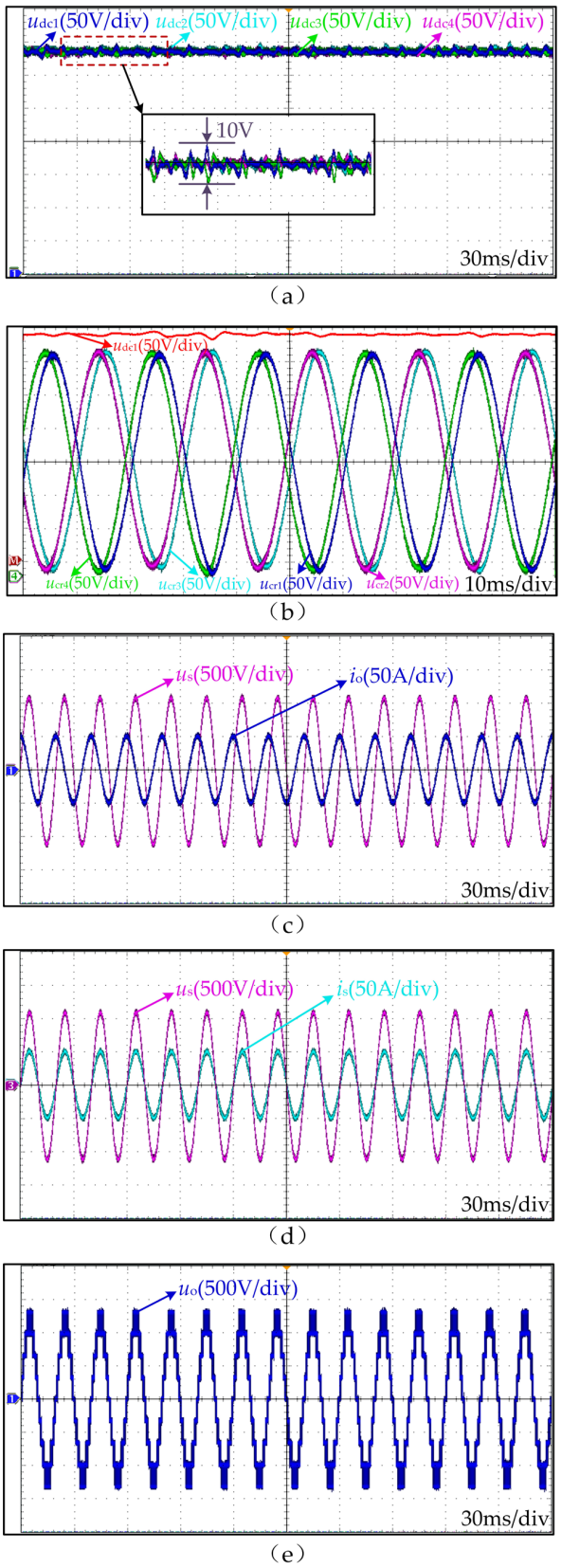


Figure 8. Steady state experimental output waveforms of the proposed novel cascaded H-Bridge STATCOM. (**a**) Experimental waveforms of individual module DC-side voltages. (**b**) Experimental waveforms of decoupling capacitor voltages and their corresponding DC-side voltages. (**c**) Experimental waveforms of output current and grid voltage. (**d**) Experimental waveforms of grid current and grid voltage. (**e**) Experimental waveform of AC-side output voltage.

As shown in the experimental waveforms of Figure 8a, with the proposed decoupling control implemented in the novel cascaded H-bridge STATCOM, the double-frequency ripple amplitude of each module's DC-side voltage is reduced to approximately 3% of the set DC voltage value. The double-frequency ripple is effectively suppressed, demonstrating significant decoupling performance. After generating a fundamental-frequency common-mode voltage, the decoupling capacitor voltages exhibit the experimental waveforms shown in Figure 8b. The upper and lower decoupling capacitor voltages on the same side display symmetrical waveforms, while those on the opposite side are asymmetrical. However, all decoupling capacitor voltages maintain a consistent fluctuation range with amplitudes of approximately 332 V. Furthermore, they satisfy the safe operating condition of $0 < u_{crx}$ (x = 1, 2, 3, 4) $< u_{dc_min}$, thereby achieving rapid suppression of the double-frequency ripple in the DC-side voltage.

Furthermore, the experimental waveforms in Figure 8c,d demonstrate that the output current i_o leads the grid voltage u_s, which aligns with the inductive load compensation setting. Meanwhile, the grid current i_s remains in phase with the grid voltage u_s, indicating that the system achieves complete compensation of reactive power with a power factor approaching unity. As shown in the waveform of Figure 8e, the AC-side output voltage exhibits excellent nine-level characteristics with significantly improved waveform quality, thus indirectly verifying the effectiveness of this decoupling scheme.

Figure 9a shows the FFT analysis results of the low-frequency band for the DC-side voltage waveform in the conventional cascaded H-bridge STATCOM based on the structure presented in Figure 7a. It can be observed that the DC-side voltage exhibits a significant 100 Hz component. Figure 9b presents the FFT analysis results of the low-frequency band for the DC-side voltage waveform in the novel cascaded H-bridge STATCOM based on the structure shown in Figure 8a. As shown, the 100 Hz component in the DC-side voltage is effectively suppressed and nearly eliminated after decoupling, thus verifying the excellent decoupling performance of the proposed novel cascaded H-bridge STATCOM.

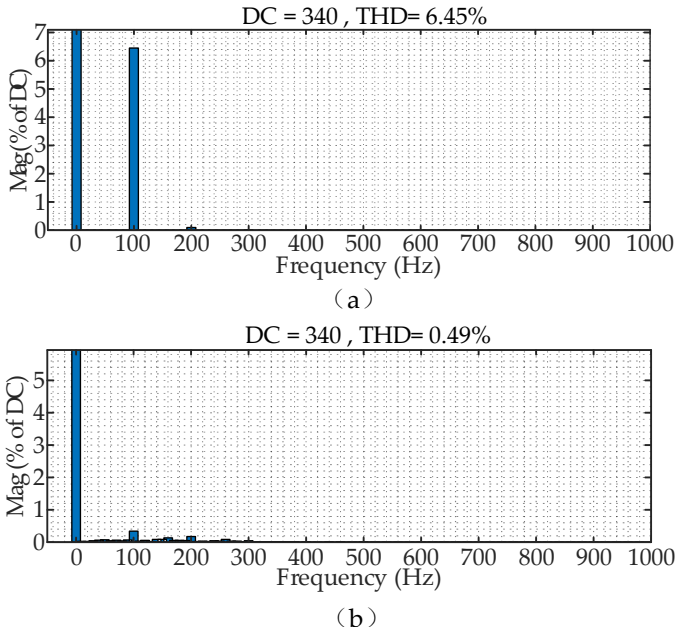


Figure 9. Low-frequency FFT analysis of DC-side voltage experimental waveforms. (**a**) Conventional cascaded H-Bridge STATCOM. (**b**) Proposed novel cascaded H-Bridge STATCOM.

Based on the experimental parameters, Figure 10 presents the experimental waveforms of the output current i_o, the decoupling inductor current i_{Lr1}, and the left bridge arm current i_l for the proposed novel cascaded H-bridge STATCOM. As can be observed from the results, the experimental current waveforms match the simulation waveforms, which further verifies the validity of the theoretical analysis. When compensating for inductive reactive loads, the bridge arm current magnitude is lower than the output current magnitude, indicating that the current stress on the switching devices is reduced compared to conventional switching devices, which can lower the cost of device selection.

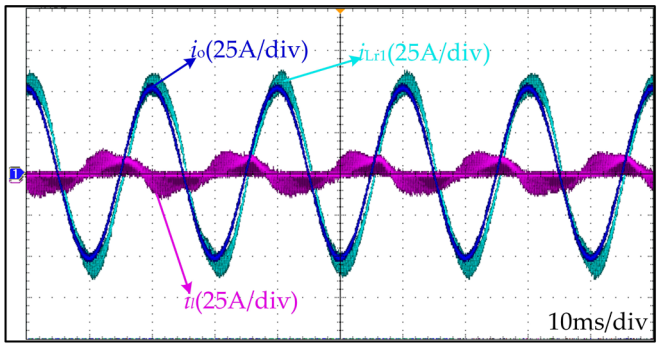


Figure 10. Proposed current experimental waveforms.

To verify the robustness of the proposed control method under load variations, Figure 11 presents the experimental output waveforms of the proposed novel cascaded H-bridge static synchronous compensator under a sudden load change at rated conditions. It can be observed that under both light-load and full-load operating conditions, the DC-side voltage maintains minimal fluctuations and the output current exhibits no significant distortion, indicating that the proposed control method achieves effective ripple suppression. Upon load variation, the proposed control method demonstrates a rapid response, enabling the system to maintain stable operation with a smooth transient process. These results fully confirm the favorable robustness of the proposed control method.

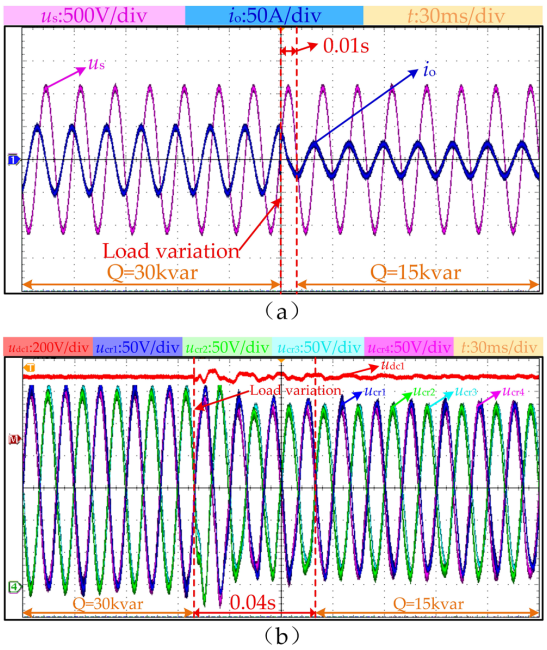


Figure 11. Experimental output waveforms under variable load conditions. STATCOM. (**a**) Experimental waveforms of output current and grid voltage. (**b**) Experimental waveforms of decoupling capacitor voltages and their corresponding DC-side voltages.

7. Conclusions

This paper proposes a novel active power decoupling cascaded H-bridge STATCOM, systematically elaborating its topology, operating principle, control method, and key parameter design, with performance verified through simulations and experiments. Results demonstrate that the proposed topology and its control method can effectively suppress the double-frequency ripple in the DC-side voltage, thereby improving the system power quality. The main conclusions are presented as follows.

(1) This topology enables suppression of the double-frequency ripple in the DC-side voltage without adding extra switching devices or DC-link-supporting capacitors, thereby effectively reducing system cost and improving the utilization rate of decoupling capacitors.
(2) By constructing a fundamental-frequency common-mode voltage across the decoupling capacitors, this method compensates for the double-frequency component without introducing additional low-frequency ripples, achieving high decoupling accuracy.
(3) By adopting an active power decoupling structure with dual bridge-arm multiplexed in the DC-SC circuit, the current stress on switching devices is effectively reduced, thereby facilitating reduced device selection difficulty and system cost.

The proposed scheme imposes an engineering constraint regarding the consistency of decoupling capacitor values, requiring strict control over capacitor matching to prevent the generation of fundamental frequency power. Finally, more detailed investigations into capacitor parameter variations in the proposed topology and grid integration issues will be addressed in subsequent work.

Author Contributions: Conceptualization, Q.F. and F.Z.; methodology, Q.F. and C.L.; validation, C.L. and X.H.; investigation, X.H. and D.L.; data curation, F.Z.; writing—original draft preparation, Q.F. and W.X.; writing—review and editing, F.Z. and C.L.; supervision, D.L. and W.X.; project administration, X.H. and D.L. All authors have read and agreed to the published version of the manuscript.

Funding: This research was funded by the Key Science and Technology Project of China Southern Power Grid Co. (GZKJXM20232507).

Data Availability Statement: The data presented in this study are available on request from the corresponding author. The data are not publicly available due to project data restriction.

Acknowledgments: Thanks to China Southern Power Grid for supporting this research.

Conflicts of Interest: Author Qihui Feng, Chenghui Lin, Xue Han and Weilong Xiao were employed by the company Electric Power Research Institute of Guizhou Power Grid Co., Ltd. Author Feng Zhu was employed by the company XJ Electric Co., Ltd. Author Dingguo Li was employed by the company Guiyang Power Supply Bureau of Guizhou Power Grid Co., Ltd. All the authors declare that the research was conducted in the absence of any commercial or financial relationships that could be construed as a potential conflict of interest.

Abbreviations

The following abbreviations are used in this manuscript:

APD	Active power decoupling
DC-SC	DC split capacitor
STATCOM	Static Synchronous Compensator
PCC	Point of Common Coupling

KVL	Kirchhoff's Voltage Law
KCL	Kirchhoff's Current Law
RC	Resonance controller

References

1. Yang, S.; Shan, T.; Yang, X. Interpretable DWT-1DCNN-LSTM Network for Power Quality Disturbance Classification. *Energies* **2025**, *18*, 231. [CrossRef]
2. Teng, X.; Tan, C.; Chang, L.; Zhang, X.; Cao, R. Review and Prospect of Research on Active Power and Frequency Control in Power System with High Proportion of Renewable Energy. *Autom. Electr. Power Syst.* **2023**, *47*, 12–35.
3. Wang, X.; Chen, X.F.; Ding, L.; Tse, C.K.; Hui, S.Y.R. Constant Output Voltage Three-Phase Capacitive-Power-Transfer Converters With Phase Expansion and Design Methods. *IEEE Trans. Power Electron.* **2026**, 1–12. [CrossRef]
4. Casado–Machado, F.; Martinez-Ramos, J.L.; Barragan-Villarejo, M.; Rosendo-Macias, J.A. Reduced Reference Frame Transform: Deconstructing Three-Phase Four-Wire Systems. *IEEE Access* **2020**, *8*, 143021–143032. [CrossRef]
5. Kahingala, T.D.; Perera, S.; Jayatunga, U.; Agalgaonkar, A.P. Network-Wide Influence of a STATCOM Configured for Voltage Unbalance Mitigation. *IEEE Trans. Power Deliv.* **2020**, *35*, 1602–16053. [CrossRef]
6. Lu, D.; Wang, J.; Yao, J.; Wang, S.; Zhu, J.; Hu, H.; Zhang, L. Clustered Voltage Balancing Mechanism and its Control Strategy for Star-Connected Cascaded H-Bridge STATCOM. *IEEE Trans. Ind. Electron.* **2017**, *64*, 7623–7633. [CrossRef]
7. Peng, Z. Simulation Research on Direct Power Control of STATCOM. *Power Syst. Big Data* **2016**, *19*, 1–5.
8. Song, J.; Duan, B.; Li, X.; Wan, D.; Ding, W.; Zhang, C.; Du, C. A modified space vector modulation for DC-side current ripple reduction in high-frequency link matrix converter. *IEEE Trans. Transp. Electrif.* **2022**, *8*, 4470–4481. [CrossRef]
9. Peng, X.; Xiao, F.; Tu, C.; Wang, L. A Fault-Tolerant Control for Hybrid Active Neutral-Point-Clamped Converters With Shared Redundant Unit Under Multiswitch Open-Circuit Fault. *IEEE Trans. Ind. Electron.* **2025**, *72*, 8550–8560. [CrossRef]
10. Patro, S.K.; Shukla, A. Enhanced parallel hybrid converter with dc ripple minimization control. *IEEE Trans. Ind. Electron.* **2019**, *67*, 9969–9975. [CrossRef]
11. Wang, H.; Wang, H.; Zhu, G.; Blaabjerg, F. An Overview of Capacitive DC-Links-Topology Derivation and Scalability Analysis. *IEEE Trans. Power Electron.* **2020**, *35*, 1805–1829. [CrossRef]
12. Ge, X.; Gao, F. Flexible third harmonic voltage control of low capacitance cascaded H-bridge STATCOM. *IEEE Trans. Power Electron.* **2018**, *33*, 1884–1889. [CrossRef]
13. Zhang, R.; Wang, S.; Ma, J.; Wang, P.; Qin, K.; Li, J.; Liu, T. Centralized active power decoupling method for the CHB converter with reduced components and simplified control. *IEEE Trans. Power Electron.* **2023**, *39*, 47–52. [CrossRef]
14. Liu, Y.; Zhang, W.; Sun, Y.; Su, M.; Xu, G.; Dan, H. Review and Comparison of Control Strategies in Active Power Decoupling. *IEEE Trans. Power Electron.* **2021**, *36*, 14436–14455. [CrossRef]
15. Wang, J.; Kang, Y.; Yao, Q.; Gillbanks, J.; Zhao, X. An efficient power decoupling topology circuit based on a novel three-port three-switches flyback series circuit. *PLoS ONE* **2024**, *19*, e0308123.
16. Takaoka, N.; Takaoka, H.; Itoh, J. Power decoupling method for isolated DC to single-phase AC converter using matrix converter. In Proceedings of the 40th Annual Conference of the IEEE Industrial Electronics Society (IECON 2014), Dallas, TX, USA, 29 October–1 November 2014; pp. 3337–3343.
17. Jia, G.; Chen, M.; Tang, S.; Zhang, C.; Zhu, G. Active Power Decoupling for a Modified Modular Multilevel Converter to Decrease Submodule Capacitor Voltage Ripples and Power Losses. *IEEE Trans. Power Electron.* **2021**, *36*, 2835–2851. [CrossRef]
18. Tang, Y.; Blaabjerg, F. A component-minimized single-phase active power decoupling circuit with reduced current stress to semiconductor switches. *IEEE Trans. Power Electron.* **2015**, *30*, 2905–2910. [CrossRef]
19. Krein, P.T.; Balog, R.S.; Mirjafari, M. Minimum energy and capacitance requirements for single-phase inverters and rectifiers using a ripple port. *IEEE Trans. Power Electron.* **2012**, *27*, 4690–4698. [CrossRef]
20. Gautam, A.R.; Fulwani, D.M.; Makineni, R.R.; Rathore, A.K.; Singh, D. Control Strategies and Power Decoupling Topologies to Mitigate 2ω-Ripple in Single-Phase Inverters: A Review and Open Challenges. *IEEE Access* **2020**, *8*, 147533–147559. [CrossRef]
21. Tang, Y.; Zhu, D.; Jin, C.; Wang, P.; Blaabjerg, F. A three-level quasi-two-stage single-phase PFC converter with flexible output voltage and improved conversion efficiency. *IEEE Trans. Power Electron.* **2014**, *30*, 717–726. [CrossRef]
22. Cao, X.; Zhong, Q.; Ming, W. Ripple Eliminator to Smooth DC-Bus Voltage and Reduce the Total Capacitance Required. *IEEE Trans. Ind. Electron.* **2015**, *62*, 2224–2235. [CrossRef]
23. Peng, Z.; Xiao, F.; Tu, C.; Wang, L.; Yuan, Y.; Tang, Y.; Guo, X. Optimal Control Strategy for LVRT and Quasi-Synchronous Droop-Controlled Inverter Considering Voltage Drop on the Distribution. *Prot. Control Mod. Power Syst.* **2026**, *11*, 144–158. [CrossRef]
24. Xie, S.; Sun, Y.; Lin, J.; Li, X.; Su, M.; Liu, Y.; Xiong, W. Adaptive power decoupling control for single-phase converter with unbalanced DC-split-capacitor circuit. *IEEE Trans. Power Electron.* **2021**, *36*, 12127–12136. [CrossRef]

25. Sun, Y.; Liu, Y.; Su, M.; Xiong, W.; Yang, J. Review of active power decoupling topologies in single-phase systems. *IEEE Trans. Power Electron.* **2016**, *31*, 4778–4794. [CrossRef]
26. Yao, W.; Wang, X.; Loh, P.C.; Zhang, X.; Blaabjerg, F. Improved power decoupling scheme for a single-phase grid-connected differential inverter with realistic mismatch in storage capacitances. *IEEE Trans. Power Electron.* **2017**, *32*, 186–199. [CrossRef]
27. Yao, W.; Loh, P.C.; Tang, Y.; Wang, X.; Zhang, X.; Blaabjerg, F. A Robust DC-Split-Capacitor Power Decoupling Scheme for Single-Phase Converter. *IEEE Trans. Power Electron.* **2017**, *32*, 8419–8433. [CrossRef]

Disclaimer/Publisher's Note: The statements, opinions and data contained in all publications are solely those of the individual author(s) and contributor(s) and not of MDPI and/or the editor(s). MDPI and/or the editor(s) disclaim responsibility for any injury to people or property resulting from any ideas, methods, instructions or products referred to in the content.